Journal of Applied Physics

Evidence of weak antilocalization in quantum interference effects of (001) oriented $La_{0.7}Sr_{0.3}MnO_3$–$SrRuO_3$ superlattices

Cite as: J. Appl. Phys. **128**, 033906 (2020); https://doi.org/10.1063/5.0014909
Submitted: 22 May 2020 . Accepted: 02 July 2020 . Published Online: 16 July 2020

Roshna Sobhanan Helen, Wilfrid Prellier, and Prahallad Padhan

Journal of Applied Physics ARTICLE scitation.org/journal/jap

Evidence of weak antilocalization in quantum interference effects of (001) oriented $La_{0.7}Sr_{0.3}MnO_3$–$SrRuO_3$ superlattices

Cite as: J. Appl. Phys. **128**, 033906 (2020); doi: 10.1063/5.0014909
Submitted: 22 May 2020 · Accepted: 2 July 2020 ·
Published Online: 16 July 2020

Roshna Sobhanan Helen,[1] Wilfrid Prellier,[2] and Prahallad Padhan[1,a)]

AFFILIATIONS

[1]Department of Physics, Indian Institute of Technology Madras, Chennai 600036, Tamilnadu, India
[2]Laboratoire CRISMAT, CNRS UMR 6508, ENSICAEN, 6 Bd du Marechal Juin, F-14050 Caen Cedex, France

[a)]**Author to whom correspondence should be addressed:** padhan@iitm.ac.in

ABSTRACT

Quantum corrections to conductivity in the ferromagnetic $La_{0.7}Sr_{0.3}MnO_3$ (LSMO) and $SrRuO_3$ (SRO) thin films depend on the structural mismatches and interfaces accommodating ions and their spins. Here, by making interfaces of LSMO and SRO in the form of artificial superlattices, we achieve positive magnetoresistance (MR) and weak antilocalization (WAL), although the individual component shows negative MR and weak localization (WL). The [20 unit cell (u.c.) LSMO/3 u.c. SRO]$_{\times 15}$ superlattice stabilizes in tetragonal symmetry associated with the rhombohedral and orthorhombic structures and demonstrates the occurrence of the single magnon scattering process. The low-field MR of the superlattice fit to the Hikami–Larkin–Nagaoka expression yields 595 Å phase coherence length (l_ϕ) with WAL of carriers. As the SRO layer thickness in the superlattice increases to 5 u.c., the value of $l_\phi = 292$ Å decreases, and positive MR increases confirm the manifestation of WAL by SRO. The orthorhombic symmetry of the SRO is preserved in the [20 u.c. SRO/3 u.c. LSMO]$_{\times 15}$ superlattice, which shows the existence of locally cooperative bond-length fluctuations and conduction due to the scattering of the electron by the Fermi liquid electrons, bond length, and spin fluctuations. However, as the LSMO layer thickness in the superlattice is increased to 5 u.c., the WL effect suppresses WAL at the low field. The spin–orbit coupling associated with magnetic anisotropy, i.e., spin and bond length fluctuations, modifies the WL in the superlattices and leads to WAL, thereby achieving positive MR.

I. INTRODUCTION

The transport properties of the materials with carriers' mean free path larger than the Fermi wavelength are described by the semiclassical Boltzmann approach. In general, the low-temperature carriers' transport in these materials is influenced by the scattering of carriers through lattice imperfections and carrier–carrier scattering. In the thin films or heterostructures, as the disorder induced by the strain or interfaces increases, the mean free path shrinks and eventually may become comparable to the Fermi wavelength. In this situation, a fully quantum-mechanical treatment, accounting for the wavelike nature of the carriers, must be applied to conductivity. This approach consists of adding some correcting terms to low-temperature conductivity, the so-called quantum corrections to conductivity (QCC).[1,2] Recently, QCC in manganites has been intensively investigated to interpret low-temperature resistivity. Generally, QCC leads to correction to resistivity from two different sources: (i) electron–electron interaction and subsequent modification of the density of states at the Fermi energy and (ii) weak localization (WL) effect arising from the self-interference of the wave pockets as they are backscattered coherently by the impurities or other defects.[1] These two contributions in the temperature-dependent conductivity of the 2D systems are of comparable magnitude. However, the contributions in the field dependence of low-temperature conductivity are radically different, and in principle, it can unambiguously determine the nature of QCC.[1,3] The external magnetic field suppressed the WL contribution as the field destroys the wave coherence, and thus, the self-interference effects are reduced, and the resistance is decreased, i.e., a negative magnetoresistance (MR) is observed. On the other hand, the influence of the field on the electron–electron scattering contribution leads to a positive magnetoresistance originated by the spin splitting of electrons in a magnetic field and by the orbital effects.

The other possible mechanism for the observed positive MR in the metallic double perovskite oxides is that the external magnetic field suppresses the long-range antiferromagnetic order to form short-range antiferromagnetic fluctuations, which enhance electronic scattering and lead to giant positive MR.[4] In contrast, the application of the magnetic field on the perovskite oxides decreases the local spin disorder and thus decreases resistivity, which leads to negative MR.[5] Even though the MR of the individual ferromagnetic perovskite oxide is negative, the positive MR feature is observed due to the structural or magnetic distortion at the thin film or heterostructure interfaces of the perovskite oxides. The positive MR $\sim$ 25% at 80 K under 4 T field observed in the $Fe_3O_4/SrTiO_3/La_{0.7}Sr_{0.3}MnO_3$(LSMO) heterostructure is attributed to the inverse correlation between the orientations of the carrier spins (states near the Fermi level) in the two ferromagnetic layers.[6] The $La_{0.9}Sr_{0.1}MnO_3/SrNb_{0.01}Ti_{0.99}O_3$ p–n junctions at 290 K under 0.01 T exhibits $\sim$ 23% MR, which is explained by the interface induced change on the concentration of the carriers and the density of state of the electrons at the Fermi level.[7] The degenerate semiconducting $SrTiO_3$ single crystals capped with ultrathin $SrTiO_3/LaAlO_3$ bilayers at a temperature of 2 K and a magnetic field of 9 T show positive MR of $>$ 30 000% due to the inhomogeneity of the materials and Lorentz type conduction.[8] The positive MR is observed in the antiferromagnetically coupled $La_{2/3}Ba_{1/3}MnO_3$ in the $La_{2/3}Ba_{1/3}MnO_3/LaNiO_3$ superlattices.[9] The low field positive MR has also been observed in the $La_{0.7}Sr_{0.3}MnO_3/SrRuO_3$,[10] and $SrMnO_3/SrRuO_3$(SRO),[11] superlattices. In this article, we report the effect of stacking order of $La_{0.7}Sr_{0.3}MnO_3$ (LSMO) and $SrRuO_3$ (SRO) on the crystal structure and MR of the $La_{0.7}Sr_{0.3}MnO_3$–$SrRuO_3$ superlattices grown on the (001) oriented $SrTiO_3$ (STO).–

II. EXPERIMENTAL METHODS

A multitargeted pulsed laser deposition system was used to grow the superlattices consisting of LSMO and SRO on (*00l*) oriented $SrTiO_3$ using a pulsed KrF excimer laser ($\lambda = 248$ nm). These superlattices were grown at a substrate temperature of 720 °C with oxygen partial pressure of 300 mTorr followed by cooling to room temperature in the presence of oxygen. The deposition rates for the SRO and LSMO layers are calibrated individually for each laser pulse of energy density $\sim$ 3 J/cm^2, and it seems to be almost the same $\sim$ 0.73 Å/pulse. A series of superlattices with [20 u.c. (unit cell) LSMO/n (=3 and 5) u.c. SRO] and [20 u.c. SRO/n u.c. LSMO] bilayer configurations were prepared by repeating the bilayer 15 times. A four-circle x-ray diffractometer was used to characterize the crystal structure of these superlattices. The Raman spectra were recorded by using a Jobin-Yvon LabRAM HR800UV spectrometer instrument equipped with a highly efficient thermo-electrically cooled charge-coupled device. The spectra were recorded at various temperatures in the backscattering configuration using a 633 nm emission line of a He–Ne laser. A physical property measurement system was used to study the electronic transport of the superlattices.

III. RESULTS AND DISCUSSION

The lattice mismatch between the substrate STO ($a = 3.905$ Å) and the LSMO ($a_{pc} = 3.88$ Å) is -0.64%, which is equal and opposite to that of the STO and SRO ($a_{pc} = 3.93$ Å). Thus, the (002) superlattice peak of [20 u.c. LSMO/5 u.c. SRO]$_{\times 15}$ appears at a higher angle, while that of [20 u.c. SRO/5 u.c. LSMO]$_{\times 15}$ appears at a lower angle as compared to that of the STO [Figs. 1(a) and 1(b)]. The θ–2θ x-ray diffraction (XRD) patterns of different superlattices show only (00*l*) peaks of the substrate and the constituents. The observed (002) Bragg's reflections with four orders of satellite peaks [Figs. 1(a) and 1(b)] on either side of the STO peaks are suggesting the presence of long-range periodicity, epitaxy, and good crystallinity. The broadness of the satellite peaks is due to the merging of Kiessig fringes.[12] The simulated XRD profile included in Figs. 1(a) and 1(b) was obtained using the DIFFaX program,[12,13] which is in good agreement with the measured XRD with respect to the position of Bragg's peaks and their relative diffracted intensity. The satellite peak positions obtained from the XRD patterns of the superlattice series are used to calculate the superlattice period (Λ). The Λ values are in good agreement with the designed thickness configurations as well as the values obtained from the fit using DIFFaX.[13]

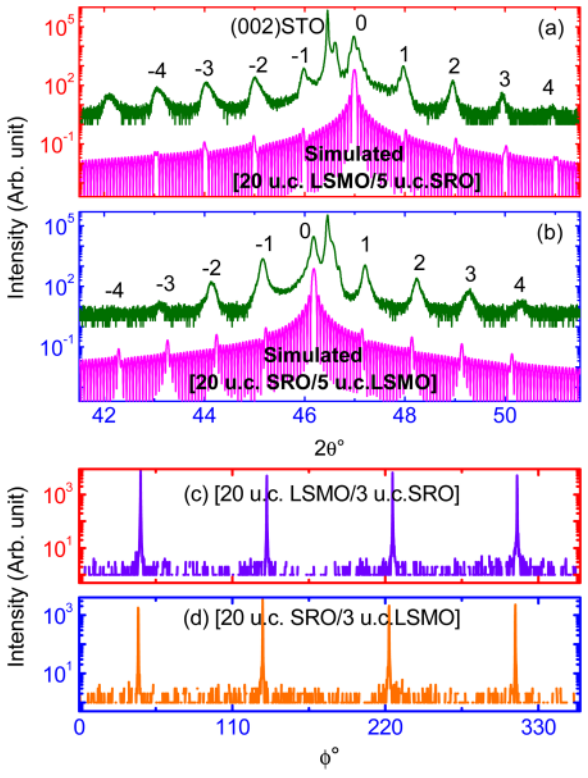

FIG. 1. θ – 2θ x-ray diffraction pattern of (a) [20 u.c. LSMO/5 u.c. SRO]$_{\times 15}$ and (b) [20 u.c. SRO/5 u.c. LSMO]$_{\times 15}$ superlattices. The (002) Bragg's reflection of STO, as well as the satellite peaks (0th and ±4th orders), is indicated. The diffraction profile of these superlattices calculated using the DIFFAX program is also shown. ϕ scan of the (103) of the (c) [20 u.c. LSMO/3 u.c. SRO]$_{\times 15}$ and (d) [20 u.c. SRO/3 u.c. LSMO]$_{\times 15}$ superlattices.

The ϕ-scan XRD patterns around $(103)_{pc}$ of $[20\text{ u.c. LSMO}/3\text{ u.c. SRO}]_{\times 15}$ and $[20\text{ u.c. SRO}/3\text{ u.c. LSMO}]_{\times 15}$ superlattices show four peaks [Figs. 1(c) and 1(d)]. The 90° separation between the consecutive peaks in the ϕ-scan confirms that these superlattices and the substrate are of fourfold symmetry with the cube-on-cube epitaxial growth. The crystal structures of these superlattices were further studied from their reciprocal space mapped along the four ϕ-orientations. The Bragg's reflection measurements consisting of 2θ–ω coupling scans in $\{103\}_{pc}$ for different ω values were performed to construct the reciprocal space mapping (RSM) (Fig. 2).

The $[20\text{ u.c. LSMO}/3\text{ u.c. SRO}]_{\times 15}$ superlattice exhibits the same $q_\perp$ along the $\langle 103\rangle_{pc}$ of $\{103\}_{pc}$ with $c_{pc} = 3.851$ Å, which is very close to c_{pc} obtained from the $\langle 001\rangle_{pc}$ [Figs. 2(a)–2(d)]. However, c_{pc} of the $[20\text{ u.c. LSMO}/3\text{ u.c. SRO}]_{\times 15}$ superlattice is smaller than the c_{pc} of the LSMO or SRO along the $\langle 001\rangle_{pc}$; hence, both LSMO and SRO experience compressive strain. The $q_\parallel$ along the $\langle 103\rangle_{pc}$ of $\{103\}_{pc}$ of the $[20\text{ u.c. LSMO}/3\text{ u.c. SRO}]_{\times 15}$ superlattice is also the same and giving $a_{pc} = 3.968$ Å, which is larger than the lattice parameters of the LSMO and SRO. So, the LSMO and SRO experience tensile strain along the $\langle 001\rangle_{pc}$. The pseudocubic lattice parameters of the $[20\text{ u.c. LSMO}/3\text{ u.c. SRO}]_{\times 15}$ superlattices extracted from the RSM can be expressed as the tetragonal structures with the lattice parameters $a_T = 5.611$ Å and $c_T = 7.702$ Å. The RSM studies confirm that the growth of the $[20\text{ u.c. LSMO}/3\text{ u.c. SRO}]_{\times 15}$ superlattices drives the rhombohedral ($R\bar{3}m$) LSMO and orthorhombic ($Pbnm$) SRO crystal structures to the tetragonal $I4/mcm$ structure.

The $[20\text{ u.c. SRO}/3\text{ u.c. LSMO}]_{\times 15}$ superlattice exhibits the same $q_\perp$ along the $\langle 103\rangle_{pc}$ of $\{103\}_{pc}$ with $c_{pc} = 3.941$ Å, which is very close to c_{pc} obtained from the $\langle 001\rangle_{pc}$ [Figs. 2(e)–2(h)]. However, the c_{pc} of the $[20\text{ u.c. SRO}/3\text{ u.c. LSMO}]_{\times 15}$ superlattice is larger than c_{pc} of the LSMO or SRO along the $\langle 001\rangle_{pc}$; thus, both LSMO and SRO experience tensile strain. The $q_\parallel$ along the $\langle 103\rangle_{pc}$ of $\{103\}_{pc}$ of the $[20\text{ u.c. SRO}/3\text{ u.c. LSMO}]_{\times 15}$ superlattice provides $a_{pc}^{103} = 3.868$ Å, $a_{pc}^{0\bar{1}3} = 3.861$ Å, $a_{pc}^{\bar{1}03} = 3.869$ Å, and $a_{pc}^{013} = 3.882$ Å, which indicates that the in-plane lattice parameters are different but smaller than that of the LSMO or SRO. So, the in-plane lattice parameters of $[20\text{ u.c. SRO}/3\text{ u.c. LSMO}]_{\times 15}$ experience compression with orthorhombic crystal structures. The orthorhombic lattice parameters of the $[20\text{ u.c. SRO}/3\text{ u.c. LSMO}]_{\times 15}$ superlattice are $a_O = 5.47$ Å, $b_O = 5.49$ Å, and $c_O = 7.882$ Å. The RSM studies suggest that the rhombohedral ($R\bar{3}m$) LSMO and orthorhombic ($Pbnm$) SRO crystal structures in the SRO/LSMO superlattices stabilize as the distorted orthorhombic structure. The structural transformation of the LSMO and/or SRO in these superlattices instigated from the variation of bond length, tilt, and rotation of the octahedral.

The polarized Raman spectra of the (001) oriented superlattices with both the stacking order measured at 100 K are shown in Fig. 3. The first-order Raman scattering because of the cubic phase of the STO is not observed as the STO transforms into a tetragonal phase around 110 K.[14] However, the second-order process in the STO due to two-phonon scattering in the frequency range of 200 – 500 cm^{-1} is observed.[15] The Raman spectrum of $[20\text{ u.c. LSMO}/3\text{ u.c. SRO}]_{\times 15}$ with parallel (HH) polarization of the incident and scattered light shows peaks centered at around 150, 200, 252, 302, 410, and 431 cm^{-1} (curve a, Fig. 3). The peaks that appear in the Raman spectra of the $[20\text{ u.c. LSMO}/3\text{ u.c. SRO}]_{\times 15}$ superlattice after cross (HV) polarization of the incident and scattered light are 175, 240, 333, 410, and 431 cm^{-1} (curve b, Fig. 3). The peaks at 200 and 427 cm^{-1} are pronounced much more strongly with HH polarization as compared to the HV polarization spectrum. The 200 cm^{-1} has the A_{1g}

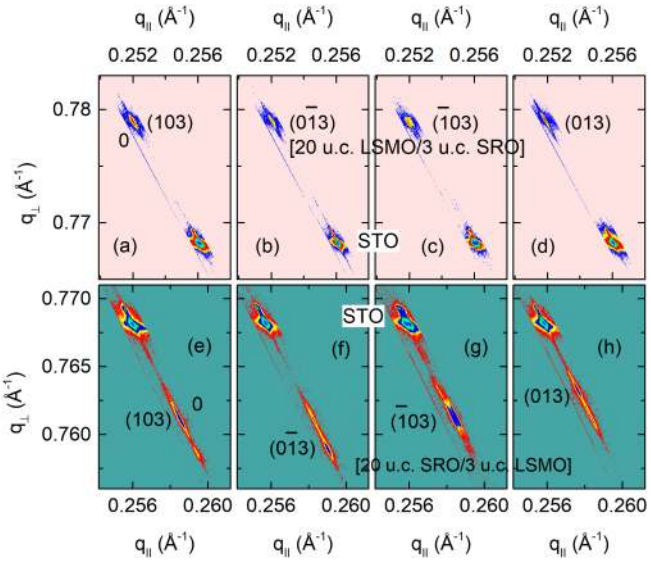

FIG. 2. Reciprocal space mapping around $\{103\}_{pc}$ plane of $[20\text{ u.c. LSMO}/3\text{ u.c. SRO}]_{\times 15}$ [panels (a) to (d)] and $[20\text{ u.c. SRO}/3\text{ u.c. LSMO}]_{\times 15}$ [panels (e) to (h)], superlattices grown on (001) STO.

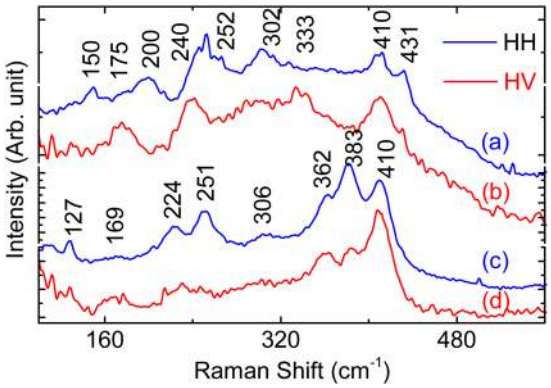

FIG. 3. Polarized Raman spectra recorded at a temperature of 100 K for the $[20\text{ u.c. LSMO}/3\text{ u.c. SRO}]_{\times 15}$ (a) and (b) and $[20\text{ u.c. SRO}/3\text{ u.c. LSMO}]_{\times 15}$ (c) and (d) superlattices grown on (001) oriented STO.

mode due to the rotation of the oxygen cage, and the 427 cm^{-1} peak has exact E_g symmetry due to the internal vibration of the oxygen cage in the rhombohedral structure of LSMO with ($R\bar{3}m$).[16] Interestingly, the A_{1g} and E_g modes are neither appearing in the HH (curve c, Fig. 3) nor HV (curve d, Fig. 3) spectra of the [20 u.c. SRO/3 u.c. LSMO]$_{\times 15}$ superlattice indicating the negligible contribution of the rhombohedral structure of 3 u.c. LSMO. The Raman peaks at 127, 224, 251, 306, and 383 cm^{-1} of the [20 u.c. SRO/3 u.c. LSMO]$_{\times 15}$ superlattice have exact A_g mode, while the peaks at 362 and 410 cm^{-1} have the B_{2g} symmetry of the constituent orthorhombic SRO in the superlattices. The peak at 169 cm^{-1} in the Raman spectrum of the [20 u.c. SRO/3 u.c. LSMO]$_{\times 15}$ superlattice neither corresponds to the orthorhombic SRO nor the rhombohedral LSMO. Considering the orthorhombic structure of LSMO, the Raman lines at 251 cm^{-1} can be assigned to A_g, while 169 and 306 cm^{-1} to B_{2g} mode.

The Raman peaks at 240, 252, and 302 cm^{-1} of the [20 u.c. LSMO/3 u.c. SRO]$_{\times 15}$ superlattice are of A_g symmetry, and the peak at 410 cm^{-1} is of B_{2g} symmetry of the orthorhombic SRO. In addition, in the Raman spectra of the [20 u.c. LSMO/3 u.c. SRO]$_{\times 15}$ superlattice, the peaks at 150 and 240 cm^{-1}(A_g), 175 and 302 cm^{-1}(B_{2g}), and 333 cm^{-1} (B_{3g}) are associated with the orthorhombic structure of the LSMO. The rhombohedral and orthorhombic structures of the LSMO and SRO, respectively, are assigned to definite atomic vibrations based on their symmetry compared to the phonon frequencies predicted by lattice dynamics calculations.[16,17] The orthorhombic structure of the LSMO matches well with the orthorhombic structure of the undoped $LaMnO_3$ compound.[16] Similar to the (011) oriented STO/[14 u.c. SRO/2 or 4 u.c. LSMO] $_{\times 15}$ (Ref. 15) and (111) oriented STO superlattices,[18] the Raman spectra of the (001) oriented STO/[20 u.c.LSMO(SRO)/3 or 5 u.c. SRO(LSMO)] $_{\times 15}$. confirm the partial reduction in symmetry of the manganite system from the rhombohedral to orthorhombic structure, which modulates the Mn–O–Mn bond angles. Such a modulation of the bond angle influences the electronic and magnetic properties of the LSMO–SRO superlattices.

The zero-field temperature-dependent resistivity ($\rho(T)$) of the [20 u.c. LSMO/3 u.c. SRO] $_{\times 15}$ superlattice is shown in the inset of Fig. 4(a). On cooling below 380 K, the resistivity of this superlattice decreases slowly, followed by a rapid decrease around its Curie temperature, and then decreases gradually down to the lowest temperature. The qualitative $\rho(T)$ behavior of this superlattice is similar to its thicker constituent LSMO. In contrast, the zero-field $\rho(T)$ of the [20 u.c. SRO/3 u.c. LSMO]$_{\times 15}$ superlattice is similar to that of the constituents SRO [inset of Fig. 4(b)]. The $\rho(T)$ of the [20 u.c. LSMO/3 u.c. SRO]$_{\times 15}$ superlattice shows metal-to-insulator transition (T_{MI}) around 335 K. T_{MI} coincides with the previous research results that T_{MI} is almost the same as T_C for the epitaxial thin film, while T_{MI} is smaller than T_C for the polycrystalline thin film.[19,20] However, T_{MI} of the [20 u.c. LSMO/3 u.c. SRO] $_{\times 15}$ superlattice is significantly smaller than its $T_C \sim$ 360 K.[21] The resistivity of the [20 u.c. LSMO/3 u.c. SRO] $_{\times 15}$ superlattice[21] in the intermediate-temperature region below T_C is explained by the double exchange[22] and phase separation[23] mechanisms in the LSMO films. The resistivity of the [20 u.c. LSMO/3 u.c. SRO]$_{\times 15}$ superlattice below 50 K is fitted with the expression,

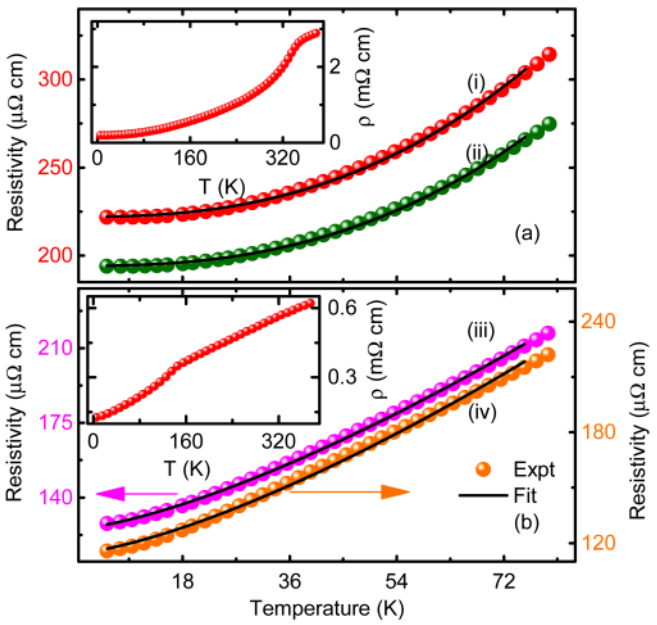

FIG. 4. Low-temperature part of the temperature-dependent resistivity of the (i) [20 u.c. LSMO/3 u.c. SRO]$_{\times 15}$, (ii) [20 u.c. LSMO/5 u.c. SRO]$_{\times 15}$, (iii) [20 u.c. SRO/3 u.c. LSMO]$_{\times 15}$, and (iv) [20 u.c. SRO/5 u.c. LSMO]$_{\times 15}$ superlattices grown on (001) oriented STO. The solid line is the fit to the data using Eq. (1). Temperature-dependent resistivity of the [20 u.c. LSMO/3 u.c. SRO]$_{\times 15}$ (inset a) and [20 u.c. SRO/3 u.c. LSMO]$_{\times 15}$ (inset b) superlattices.

$$\rho = \rho_0 + \rho_1 T^p, \tag{1}$$

where the temperature-independent term ρ_0 is the resistivity caused by domain, grain boundary, and other temperature-independent scattering mechanisms. The temperature-dependent term $\rho_1 T^p$ corresponds to the electron scattering processes, where the exponent ρ value determines the nature of the electron scattering.[5] At low temperature, a material with quadratic temperature-dependent resistivity, i.e., $\rho_1 > 0$ and $p = 2$, the transport process is dominated by electron–electron scattering.[1,24] Figure 4(a) shows ρ(T) of the [20 u.c. LSMO/3 u.c. SRO]$_{\times 15}$ superlattice and the fit of ρ(T) to Eq. (1). ρ(T) has been fitted to Eq. (1) with $p = 1.5$, 2, 2.5, 4.5, and 5, and the best fit yields $\rho_1 > 0$ and $p = 2.5$. Similar temperature-dependent resistivity has been observed in the 3d-ferromagnet,[25] $La_{1-x}Ca_xMnO_3$ (Ref. 5) and $La_{0.825}Sr_{0.175}Mn_{1-x}Cu_xO_3$.[26] The $T^{2.5}$ dependence of resistivity of the nearly half-metallic ferromagnet is explained by a single magnon scattering process, although the perfect half-metallic ferromagnet exhibits $T^{4.5}$ dependent resistivity associated with two magnon scattering processes.[27]

$\rho(T)$ of the [20 u.c. SRO/3 u.c. LSMO]$_{\times 15}$ superlattice exhibits metal-like behavior in the entire temperature range with an anomaly at around 150 K. The resistivity of the [20 u.c. SRO/3 u.c. LSMO]$_{\times 15}$ superlattice above 150 K increases almost linearly

without saturation, even in the ferromagnetic state of the superlattice, which is in contrast with the previous explanation of saturated spin fluctuation scattering in the SRO.[28] The best fit of Eq. (1) to ρ(T) of the [20 u.c. SRO/3 u.c. LSMO]$_{\times 15}$ superlattice yield $p = 1.4$ [Fig. 4(b)], which is close to the value observed in several strongly correlated systems such as $SrRuO_3$, $Na_{0.5}CoO_2$, and $CaVO_3$.[24,29] Similar temperature-dependent transport has been observed in the $LaNiO_3/LaAlO_3$ superlattice.[30] ρ(T), which follows $T^{1.5}$ dependence, is explained by modeling the scattering of conduction electrons by locally cooperative bond-length fluctuations and Fermi liquid electrons,[24] or within the framework of a self-consistent spin fluctuation theory.[31] The observed $T^{1.4}$ dependence of resistivity indicates the existence of locally cooperative bond-length fluctuations consistent with the structural distortion of the orthorhombic phase observed in the RSM as well as Raman scattering.[32] Thus, the transport in the [20 u.c. SRO/3 u.c. LSMO] $_{\times 15}$ superlattice can be attributed to the scattering of the electron by the Fermi liquid electrons, bond length, and spin fluctuations.

The qualitative behavior of $\rho(T, H)$ of the [20 u.c. LSMO/3 *u*.c. SRO] $_{\times 15}$ superlattice is similar to that of $\rho(T, 0)$ with lower ρ near T_{MI} [inset of Fig. 5(a)]. Thus, the magnetoresistance $\left(MR = \frac{\rho(T,H)-\rho(T,0)}{\rho(T,0)} \times 100\ (\%)\right)$ is negative. The MR of the [20 u.c. LSMO/3 u.c. SRO] $_{\times 15}$ superlattice is maximum near T_{MI} and is ∼ 10% under 3 T field, which is relatively smaller than that of the LSMO films grown on STO[33] [Fig. 5(a)]. The reduced MR in the superlattice as compared to the thin film of the component LSMO is attributed to the presence of non-magnetic conducting SRO. The $\rho(T, H)$ of the [20 u.c. SRO/3 u.c. LSMO] $_{\times 15}$ superlattice is similar to that of $\rho(T, 0)$ with lower ρ near the resistivity anomaly [inset Fig. 5(b)]. However, for field ≥ 3 T, the MR is positive at a temperature below 10 K but negative above 10 K. The temperature-dependent MR [MR(T, H)] of the [20 u.c. SRO/3 u.c. LSMO]$_{\times 15}$ superlattice under 7 T field exhibits peaks around 38 K, 143 K, and 310 K [Fig. 5(b)]. The MR(T, 7 T) of the [20 u.c. SRO/3 u.c. LSMO]$_{\times 15}$ superlattice shows maximum MR around 143 K, which is smaller than that of the SRO films grown on STO.[34] The presence of ferromagnetic LSMO in the [20 u.c. SRO/3 u.c. LSMO]$_{\times 15}$ superlattice reduces the MR of the SRO component, which indicates the reduction in magnetic fluctuation in the superlattice.

The isothermal out-of-plane MR of these superlattices was measured at 10 K to understand the transport properties at low temperatures. The bulk *LSMO* is well known for its colossal negative MR in the presence of the magnetic field. However, as the field increases from 0 T, the MR of the [20 u.c. LSMO/3 u.c. SRO]$_{\times 15}$ superlattice is positive and increases up to 0.7 T field. On further increasing the field above 0.7 T, the MR of the superlattice decreases to zero, becomes negative, and then decreases linearly with the increasing field [Fig. 6(a)]. The 0.7 T switching field is

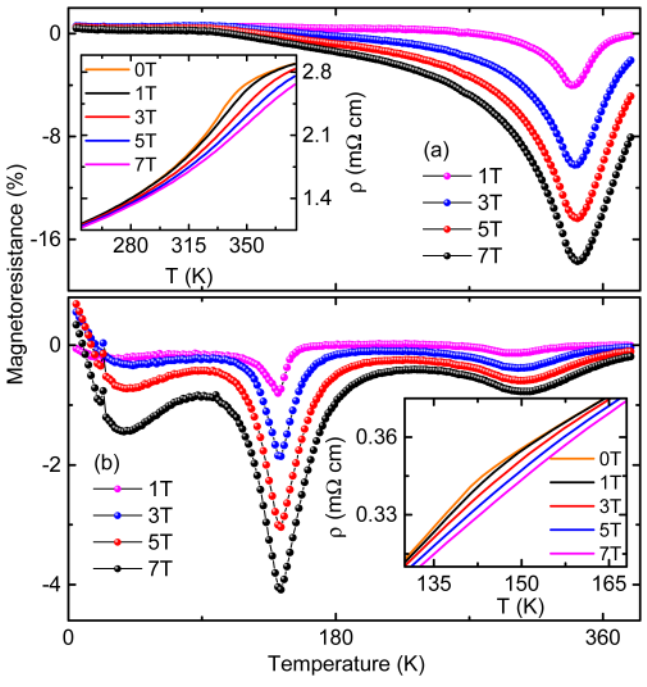

FIG. 5. Temperature-dependent magnetoresistance at various fields for the (a) [20 u.c. LSMO/3 u.c. SRO]$_{\times 15}$ and (b) [20 u.c. SRO/3 u.c. LSMO]$_{\times 15}$ superlattices grown on (001) oriented STO. Part of the temperature-dependent resistivity at various fields for [20 u.c. LSMO/3 u.c. SRO]$_{\times 15}$ (inset a) and [20 u.c. SRO/3 u.c. LSMO]$_{\times 15}$ (inset b) superlattices.

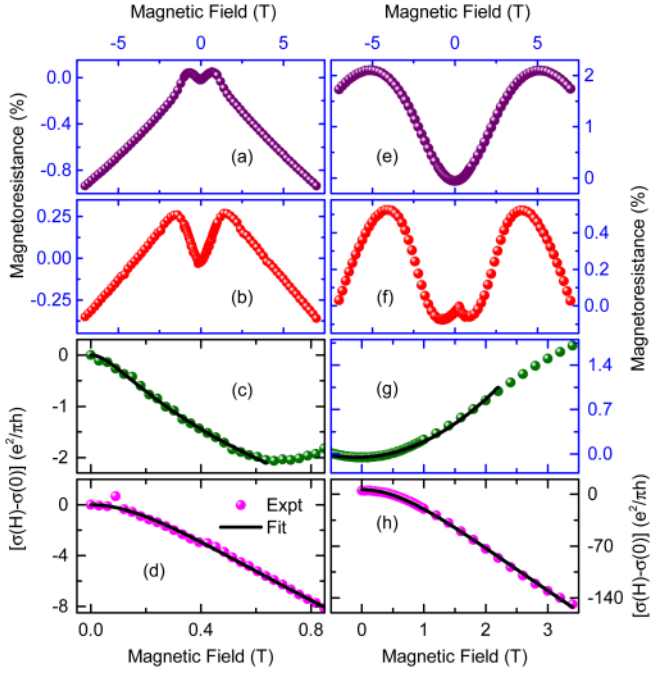

FIG. 6. Field-dependent magnetoresistance (a), (b), (e), (f), and (g) and magnetoconductance (c), (d), and (h) measured at 10 K for the (a) and (c) [20 u.c. LSMO/3 *u*.c. SRO]$_{\times 15}$; (b) and (d) [20 u.c. LSMO/5 u.c. SRO]$_{\times 15}$; (e), (g), and (h) [20 u.c. SRO/3 u.c. LSMO]$_{\times 15}$; and (f) [20 u.c. SRO/5 u.c. LSMO]$_{\times 15}$ superlattices grown on (001) oriented STO. The solid line is the HLN fit to the field-dependent Δσ at the low field in panels (c), (d), and (h). The solid line is the quadratic fit to the field-dependent MR at the low field in panel (g).

very large compared to its coercive field.[21] As the SRO layer thickness in the superlattice increases from 3 u.c. to 5 u.c., the maximum positive MR increases from 0.04% to 0.26% but the negative MR decreases. The maximum positive MR of the $[20\,\text{u.c. LSMO}/5\,\text{u.c. SRO}]_{\times 15}$ superlattice appeared at ~1.5 T switching field, and the field is almost twice that of the superlattice with 3 u.c. SRO [Fig. 6(b)]. The nature of quantum transport in the superlattice is analyzed from the change in magnetoconductance ($\Delta\sigma(H) = \sigma(H) - \sigma(0)$). $\Delta\sigma$ at the field below 0.6 T is fitted using the Hikami–Larkin–Nagaoka (HLN) theory [Fig. 6(c)]. In the HLN theory, $\Delta\sigma$ in the 2D is as follows:[35]

$$\Delta\sigma(H) = \sigma(H) - \sigma(0) = \frac{\alpha e^2}{2\pi^2\hbar}\left[\psi\left(\frac{1}{2}+\frac{\hbar}{4He l_\phi^2}\right) - \ln\left(\frac{\hbar}{4He l_\phi^2}\right)\right]. \quad (2)$$

Here, ψ is the digamma function, and α is a coefficient reflecting the strength of the spin–orbit coupling and magnetic scattering. l_ϕ represents the phase coherence length, which describes the quantum correction to conductivity in the 2D systems. $\Delta\sigma(H)$ is negative and follows Eq. (2) because of the coherent electron–electron scattering in the absence of spin–orbit coupling. Interestingly, the spin–orbit coupling adds an additional phase to the self-interference, which leads to weak antilocalization (WAL), and $\Delta\sigma(H)$ becomes positive. The solid line in Fig. 6(c) represents Eq. (2), which indicates the best fit to the positive $\Delta\sigma(H)$ of the $[20\,\text{u.c. LSMO}/3\,\text{u.c. SRO}]_{\times 15}$ superlattice endorsing the existence of the WAL. The fit yields the l_ϕ as 595 Å with WAL of charge carriers. As the SRO thickness of the superlattice is increased to 5 u.c., l_ϕ decreases to 292 Å [Fig. 6(d)]. The observed low-field WAL effect in the superlattice is in contrast to the weak localization effect reported in the LSMO thin films grown on $SrTiO_3$.[36] Nevertheless, the positive MR has been observed in the LSMO thin films grown on Si.[37] The positive MR observed in the half-metallic double perovskite Sr_2CrWO_6 thin films grown on (001) oriented $SrTiO_3$ is explained by the short-range antiferromagnetic fluctuations.[4] Propitiously, the $[20\,\text{u.c. LSMO}/3\text{ or }5\,\text{u.c. SRO}]_{\times 15}$ superlattices exhibit weak antiferromagnetic coupling along the [001] orientation of the field.[21] Thus, the positive MR in the $[20\,\text{u.c. LSMO}/3\,\text{u.c. SRO}]_{\times 15}$ superlattice can be attributed to spin–orbit coupling and weak antiferromagnetic coupling, which are influenced by the structural reconstruction, as evidenced in the RSM and Raman spectra.

For the $[20\,\text{u.c. SRO}/3\,\text{u.c. LSMO}]_{\times 15}$ superlattice, the MR is positive except in the $\pm$ 0.42 T field range, and the maximum positive MR is observed at 5.2 T [Fig. 6(e)]. As the LSMO thickness increases to 5 *u.c.*, the negative MR range increases to $\pm$ 1.4 T, the maximum positive MR appear at relatively lower field 4.2 T, and total MR reduces [Fig. 6(f)]. In addition, the MR(H) of the $[20\,\text{u.c. SRO}/5\,\text{u.c. LSMO}]_{\times 15}$ superlattice exhibits switching around $\pm$ 0.3 T, which is close to the coercive field in field-dependent magnetization. The temperature-dependent magnetization of the $[20\,\text{u.c. SRO}/5\,\text{u.c. LSMO}]_{\times 15}$ superlattice shows antiferromagnetic and ferromagnetic exchange coupling between the LSMO and SRO layers for in-plane and out-of-plane orientation of the field, respectively.[21] Thus, the presence of strong magnetic anisotropy in the superlattice forms short-range antiferromagnetic fluctuations, consistent with the consequences of the low-temperature $\rho(T)$ fitting, the proposed spin fluctuations, which is one of the possible sources to produce positive MR.[4]

The MR(H) clearly shows the change in magnetoresistance from negative to positive and its curvature back for a large enough field. The MR(H) in Fig. 6(g) shows the fit to the orbital magnetoresistance. The orbital magnetoresistance can be expressed as $\text{MR(H)} = \frac{1-(\mu H)^2}{ne\mu\,\rho(0)} - 1$. The fit yields mobility (μ) of 0.56 $\frac{m^2}{Vs}$ and carrier concentration (n) of $1.13 \times 10^{25}\,m^{-3}$, which are smaller than the reported mobility and carrier concentration of the SRO.[38] In addition, the fit diverges from the experimental data for the field larger than 2 T, i.e., the contribution of the orbital effect on the high field MR is negligible. Furthermore, the field dependence $\Delta\sigma(H \leq 3.6\ T)$ of the $[20\,\text{u.c. SRO}/3\,\text{u.c. LSMO}]_{\times 15}$ superlattice fits well to Eq. (2) with $l_\phi \sim$ 143 Å [Fig. 6(h)], suggesting the existence of the WAL. The observed WAL in the $[20\,\text{u.c. SRO}/3\,\text{u.c. LSMO}]_{\times 15}$ superlattice is in contrast with the reported WL of the SRO grown on STO.[39] As the LSMO thickness increases, $\Delta\sigma(H)$ of the $[20\,\text{u.c. SRO}/5\,\text{u.c. LSMO}]_{\times 15}$ superlattice shows a transition from WL to WAL with the increasing field. However, similar $\Delta\sigma(H)$ has been observed in the $SrIrO_3$ grown on STO[40] and $LaAlO_3//SrTiO_3/LaAlO_3$ heterostructure,[41] which is explained by the modification of weak localization by spin–orbit coupling. The positive MR of the $[20\,\text{u.c. SRO}/3\,\text{u.c. LSMO}]_{\times 15}$ superlattice is attributed to spin–orbit coupling associated with magnetic anisotropy, i.e., spin and bond length fluctuation.[42,43]

IV. CONCLUSIONS

In conclusion, quantum corrections to conductivity successfully describe the low-temperature electrical conductivity of the (001) oriented LSMO–SRO superlattices with both stacking orders. At low temperature, the $T^{1.4}$ dependent resistivity of the $[20\,\text{u.c. SRO}/3\text{ or }5\,\text{u.c. LSMO}]_{\times 15}$ superlattice indicates the existence of locally cooperative bond-length fluctuations consistent with the structural distortion of the orthorhombic phase observed in the RSM as well as Raman scattering. Thus, the transport in the $[20\,\text{u.c. SRO}/3\,\text{u.c. LSMO}]_{\times 15}$ superlattice can be attributed to the scattering of the electron by the Fermi liquid electrons, bond length, and spin fluctuations. On the other hand, the low-temperature resistivity of the $[20\,\text{u.c. LSMO}/3\text{ or }5\,\text{u.c. SRO}]_{\times 15}$ superlattice varies as $T^{2.5}$ demonstrates the occurrence of the single magnon scattering process. The HLN fit to $\Delta\sigma(H)$ of the $[20\,\text{u.c. LSMO}/3\,\text{u.c. SRO}]_{\times 15}$ superlattice at 10 K yields $l_\phi =$ 595 Å with WAL of charge carriers. As the SRO layer thickness increases, the value of $l_\phi =$ 292 Å decreases, suggesting the increase of the WAL effect and positive magnetoresistance. The low field MR of the $[20\,\text{u.c. SRO}/3\,\text{u.c. LSMO}]_{\times 15}$ superlattice at 10 K varies as H^2 and fits well with the HLN expression. However, the contribution of WAL dominates over the orbital effect. The positive MR in these superlattices is attributed to the modification of weak localization by the spin–orbit coupling. Our observations reported here about the quantum correction to conductivity in the LSMO–SRO superlattices, which confirm the occurrence of weak antilocalization because of the spin–orbit coupling induced additional phase to self-

interference. The result stimulates further theoretical and experimental work for fundamental science and technological application as quantum materials. The stabilization of the crystal structure and improvement of transport properties could pave the way for new technology for the modern spintronics based devices.

ACKNOWLEDGMENTS

We greatly acknowledge the LAFICS, DST-FIST PPMS facility, and New Faculty Seed Grant of the Indian Institute of Technology Madras.

DATA AVAILABILITY

The data that support the findings of this study are available from the corresponding author upon reasonable request.

REFERENCES

[1]P. A. Lee and T. V. Ramakrishnan, Rev. Mod. Phys. **57**(2), 287–337 (1985).
[2]B. L. Altshuler and A. G. Aronov, *Electron-Electron Interaction in Disordered Conductors* (Elsevier Science, Oxford, 1985).
[3]G. Herranz, F. Sanchez, J. Fontcuberta, V. Laukhin, J. Galibert, M. V. Garc-Cuenca, C. Ferrater, and M. Varela, Phys. Rev. B **72**(1), 14457 (2005).
[4]J. Zhang, W.-J. Ji, J. Xu, X.-Y. Geng, J. Zhou, Z.-B. Gu, S.-H. Yao, and S.-T. Zhang, Sci. Adv. **3**(11), e1701473 (2017).
[5]P. Schiffer, A. P. Ramirez, W. Bao, and S.-W. Cheong, Phys. Rev. Lett. **75**(18), 3336–3339 (1995).
[6]K. Ghosh, S. B. Ogale, S. P. Pai, M. Robson, E. Li, I. Jin, Z. Dong, R. L. Greene, R. Ramesh, T. Venkatesan, and M. Johnson, Appl. Phys. Lett. **73**(5), 689–691 (1998).
[7]H. B. Lu, S. Y. Dai, Z. H. Chen, Y. L. Zhou, B. L. Cheng, K. J. Jin, L. F. Liu, G. Z. Yang, and X. L. Ma, Appl. Phys. Lett. **86**(3), 032502 (2005).
[8]A. David, Y. Tian, P. Yang, X. Gao, W. Lin, A. B. Shah, J.-M. Zuo, W. Prellier, and T. Wu, Sci. Rep. **5**, 10255 (2015).
[9]K. R. Nikolaev, A. Y. Dobin, I. N. Krivorotov, W. K. Cooley, A. Bhattacharya, A. L. Kobrinskii, L. I. Glazman, R. M. Wentzovitch, E. D. Dahlberg, and A. M. Goldman, Phys. Rev. Lett. **85**(17), 3728–3731 (2000).
[10]M. Ziese, E. Pippel, E. Nikulina, M. Arredondo, and I. Vrejoiu, Nanotechnology **22**(25), 254025 (2011).
[11]P. Padhan and W. Prellier, Phys. Rev. B **76**(2), 24427 (2007).
[12]A. Sahoo, P. Padhan, and W. Prellier, ACS Appl. Mater. Interfaces **9**(41), 36423–36430 (2017).
[13]P. Padhan, W. Prellier, and B. Mercey, Phys. Rev. B **70**(18), 184419 (2004).
[14]R. Loetzsch, A. Lubcke, I. Uschmann, E. Forster, V. Grobe, M. Thuerk, T. Koettig, F. Schmidl, and P. Seidel, Appl. Phys. Lett. **96**, 071901 (2010).
[15]B. C. Behera, A. V. Ravindra, P. Padhan, and W. Prellier, Appl. Phys. Lett. **104**, 092406 (2014).
[16]M. N. Iliev, M. V. Abrashev, H.-G. Lee, V. N. Popov, Y. Y. Sun, C. Thomsen, R. L. Meng, and C. W. Chu, Phys. Rev. B **57**(5), 2872–2877 (1998).
[17]E. Granado, N. O. Moreno, A. Garcia, J. A. Sanjurjo, C. Rettori, I. Torriani, S. B. Oseroff, J. J. Neumeier, K. J. McClellan, S.-W. Cheong, and Y. Tokura, Phys. Rev. B **58**(17), 11435–11440 (1998).
[18]S. H. Roshna, W. Prellier, and P. Padhan, Nanoscale **12**(8), 5151–5158 (2020).
[19]M. Jain, Y. Li, M. F. Hundley, M. Hawley, B. Maiorov, I. H. Campbell, L. Civale, Q. X. Jia, P. Shukla, A. K. Burrell, and T. M. McCleskey, Appl. Phys. Lett. **88**, 232510 (2006).
[20]Y. Chen, J. Zhu, S. Zhang, X. Dong, X. Lei, X. Tang, and G. Wang, J. Am. Ceram. Soc. **94**(9), 2783–2787 (2011).
[21]P. Padhan and W. Prellier, Appl. Phys. Lett. **99**(26), 263108 (2011).
[22]C. Zener, Phys. Rev. **82**(3), 403–405 (1951).
[23]J. Tao, D. Niebieskikwiat, M. Varela, W. Luo, M. A. Schofield, Y. Zhu, M. B. Salamon, J. M. Zuo, S. T. Pantelides, and S. J. Pennycook, Phys. Rev. Lett. **103**(9), 97202 (2009).
[24]F. Rivadulla, J.-S. Zhou, and J. B. Goodenough, Phys. Rev. B **67**, 165110 (2003).
[25]B. Raquet, M. Viret, E. Sondergard, O. Cespedes, and R. Mamy, Phys. Rev. B **66**, 024433 (2002).
[26]L. Pi, L. Zheng, and Y. Zhang, Phys. Rev. B **61**, 8917 (2000).
[27]X. Wang and X.-G. Zhang, Phys. Rev. Lett. **82**, 4276 (1999).
[28]P. B. Allen, H. Berger, O. Chauvet, L. Forro, T. Jarlborg, A. Junod, B. Revaz, and G. Santi, Phys. Rev. B **53**(8), 4393–4398 (1996).
[29]L. M. Wang, H. E. Horng, and H. C. Yang, Phys. Rev. B **70**, 014433 (2004).
[30]H. Wei, M. Jenderka, M. Bonholzer, M. Grundmann, and M. Lorenz, Appl. Phys. Lett. **106**, 042103 (2015).
[31]S. G. Mishra and P. A. Sreeram, Phys. Rev. B **57**, 2188 (1998).
[32]G. Herranz, V. Laukhin, F. Sanchez, P. Levy, C. Ferrater, M. V. Garcia-Cuenca, M. Varela, and J. Fontcuberta, Phys. Rev. B **77**, 165114 (2008).
[33]Y. Wenhao, Y. Zhang, D. Cao, J. Yang, W. Bai, Y. Chen, G. Wang, X. Dong, C. Duan, and X. Tang, J. Appl. Phys. **117**, 17E102 (2015).
[34]P. Padhan, W. Prellier, and R. C. Budhani, J. Appl. Phys. **102**(4), 043909 (2007).
[35]S. Hikami, A. I. Larkin, and Y. Nagaoka, Prog. Theor. Phys. **63**(2), 707–710 (1980).
[36]W. Niu, M. Gao, X. Wang, F. Song, J. Du, X. Wang, Y. Xu, and R. Zhang, Sci. Rep. **6**, 26081 (2016).
[37]B. Das and P. Padhan, Appl. Phys. Lett. **115**, 222401 (2019).
[38]L. Braic, N. Vasilantonakis, B. Zou, S. A. Maier, N. M. Alford, A. V. Zayats, and P. K. Petrov, Sci. Rep. **5**, 9118 (2015).
[39]X. Shen, X. Qiu, D. Su, S. Zhou, A. Li, and D. Wu, J. Appl. Phys. **117**(1), 015307 (2015).
[40]L. Zhang, X. Jiang, X. Xu, and X. Hong, APL Mater. **8**, 051108 (2020).
[41]W. Lin, L. Li, F. Doğan, C. Li, H. Rotella, X. Yu, B. Zhang, Y. Li, W. S. Lew, S. Wang, W. Prellier, S. J. Pennycook, J. Chen, Z. Zhong, A. Manchon, and T. Wu, Nat. Commun. **10**, 3052 (2019).
[42]R. Gunnarsson, Phys. Rev. B **85**, 235409 (2012).
[43]A. Singh, S. Mohapatra, C. Bhandari, and S. Satpathy, J. Phys. Commun. **2**, 115016 (2018).